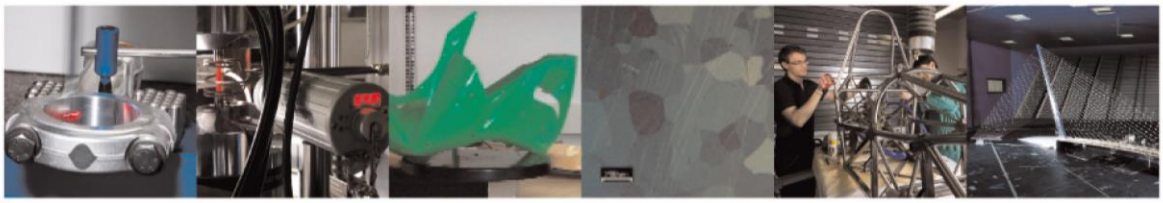

On the thermo-mechanical behavior of NiTi shape memory elements for potential smart micro-actuation applications

Biffi, CARLO ALBERTO; Bonacina, Luca; Nespoli, Andrea; Previtali, Barbara; Tuissi, Ausonio

This is a post-peer-review, pre-copyedit version of an article published in Journal of Intelligent Material Systems and Structures, Volume: 27 issue: 14, page(s): 1875-1884. The final authenticated version is available online at: http://dx.doi.org/10.1177/1045389X14566521

On the thermo-mechanical behavior of NiTi shape memory elements for potential smart micro-actuation applications

Carlo A Biffi[1], Luca Bonacina[2], Adelaide Nespoli[1], Barbara Previtali[2] and Ausonio Tuissi[1]

Introduction

Shape memory alloys (SMAs) are smart materials able to recover a pre-determinate shape after a severe deformation upon heating. At the basis of this unique property, there is a thermoelastic solid state martensitic transformation (MT) between two structures: martensite, stable at low temperature, and austenite, stable at high temperature (Funakubo, 1984; Otsuka and Wayman, 1998). The SM effect consists in the deformation (detwinning) of the martensite by applying an appropriate external load. Then, the heating, above the characteristic temperatures of the MT, permits the material to recover its original shape producing mechanical work that can be easily exploited to produce linear or rotational motion in active and smart systems, as reported by Nespoli et al. (2010b).

The high strain recovery, the possibility of designing the active element with the desired geometry, and the easiness of the device are important features that make the SMAs suitable for the development of different scales of actuators (Nespoli et al., 2012a). In the mini- and micro-scales, these materials find many applications as they present the highest power-to-weight ratio as function of the actuator weight (Ikuta, 1990). In details, mini-scale SMA actuators were studied in different configurations, showing their potentialities in function of the motion to be realized (Nespoli et al., 2010a, 2012b).

Furthermore, the use of SMAs in micro-systems improves the dynamic response of the component, because a higher surface-to-volume ratio can cause a faster cooling (Bellouard et al., 2008; Kohl and Skrobanek, 1998). For realizing features in the micro-size order, laser machining is one of the most exploited

[1]National Research Council—Institute for Energetics and Interphases (CNR-IENI), Lecco, Italy
[2]Department of Mechanical Engineering, Politecnico di Milano, Milano, Italy

Corresponding author:
Carlo A Biffi, National Research Council—Institute for Energetics and Interphases (CNR-IENI), C.so Promessi Sposi 29, 23900 Lecco, Italy.
Email: carlo.biffi@ieni.cnr.it

fabrication processes, as shown in the work reported by Kohl et al. (2002), because of its high productivity and repeatability, good quality, and great level of industrialization. The literature offers a lot of examples of laser material processing on SMAs, since their peculiar properties make conventional machining often not applicable (Schuessler, 2000). Several open literature works deal on studying the effect of the principal process parameters: pulse duration (Li et al., 2006), emission wavelength (Yung et al., 2005), and power (Pfeifer et al., 2010). Because of the heat flow associated with the laser beam, this technology produces thermal damages (i.e. melted material and heat affected zone) and surface defects (i.e. oxides) that compromise the final functional properties. For this reason, laser machining has to be followed by some post-processing to recover the SMA functional properties (Nespoli et al., 2014). Previous studies demonstrated that these defects can partially inhibit the detwinning of the martensite, causing an obstacle to the MT for the precipitation of different phases (Biffi et al., 2012, 2014; Previtali et al., 2010; Tuissi et al., 1999).

Hence, it has been proposed that post-processing (i.e. chemical and electrochemical polishing) is usually sufficient to remove these unwanted defects from the SMA elements (Biffi et al., 2013; Nespoli et al., 2014).

In this work, the authors studied the functional behavior of micro-elements in NiTi SMA, which can be adopted as promising active elements for smart actuation in micro-systems. Instead of using a thin wire shape according to classical applications, here a sinusoidal-like shape has been laser micro-machined from a thin NiTi plate and then the micro-elements were chemical etched, as reported by Biffi et al. (2013). The aim of this work is the evaluation of the functional response of these micro-elements, showing how they can be properly used for smart micro-actuation devices.

In order to identify the operating temperature range, calorimetric characterization was proposed in the final material condition. Then, two types of thermo-mechanical tests were done for evaluating the functional behavior of the micro-elements: tensile test and displacement recovery test. The tensile test results were thus used as input stress–strain characteristics in the numerical modeling. Strain recovery testing, on the contrary, showed the functional performances in actuation of these micro-elements.

Finally, the stress distribution in the micro-elements was numerically evaluated through finite element modeling (FEM) in both austenite and martensite phases.

Sample preparation and experimental characterization

SM micro-elements were realized by using a NiTi alloy ($Ni_{50.3}Ti_{49.7}$ at.%); the material was produced, at

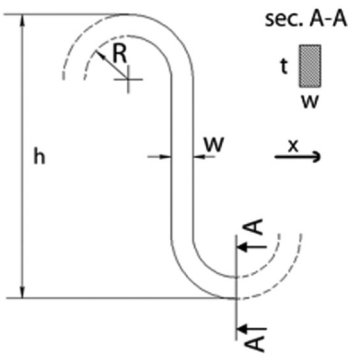

Figure 1. Schematic of the elementary geometry.

CNR-IENI Lecco laboratory, by vacuum induction melting. The ingot produced was hot and cold rolled down to tapes of 140 μm in thickness (final cold deformation of 30% in thickness reduction). Then, the NiTi tapes were thermally treated at 400°C for 15 min, followed by water quenching at room temperature to promote the one-way SM effect. Surface oxides of the sheet were removed by a chemical etching solution of 50% water, 40% HNO_3, and 10% HF.

The NiTi tapes were laser patterned by means of a nanosecond fiber laser, at Department of Mechanical Engineering of Politecnico di Milano. Several samples were prepared. The elementary geometry (see Figure 1) was replicated in function of the number of curvatures M (where M = 1, 3, 5), along the rolling direction of the tapes, as shown in Figure 2. The characteristic dimensions of the elementary geometry are listed in Table 1.

The process parameters, adopted for NiTi laser micro-cutting, were reported elsewhere (Biffi et al., 2013; Nespoli et al., 2014). An additional chemical etching for 4 min at 30°C, inside ultrasonic cleaner, was performed on processed NiTi micro-elements.

Transformation temperatures of small specimens (about 0.2 mg weight) were investigated by means of a differential scanning calorimetry (DSC) (Q100 TA Inst.), within the temperature range (−100°C; + 100°C) at a rate of 10°C/min; during this test, the sample weight was about 0.18 mg. Thermo-mechanical properties of the micro-samples were measured by a dynamic mechanical analyzer (DMA) (Q800 TA Inst.). Two kinds of mechanical tests were carried out. The first one consists in a standard tensile test in both martensite and austenite temperatures. The second mechanical analysis is a strain recovery test as a function of temperature under different constant loads. Comparison between the functional properties as a function of the number of curvatures M (M = 1, 3, 5) was also considered.

Model definition for FE analysis

To evaluate the stress distribution in the micro-elements during a tensile test, an FE approach was adopted.

Finite element analysis (FEA) was performed using ABAQUS 6.9 code to evaluate the stress distribution in the micro-elements, in function of the operating temperatures (material state) and geometry.

Quadratic hexahedral elements, characterized by an additional node in the middle of the edge for higher resolution, were adopted for a uniform discretization of the geometry. Element size was fixed to 0.03 mm in order to guarantee the convergence of the solution. A distributed load was applied on the transversal section of the free extreme side of the micro-element.

Due to the dimensions in the micro range, which are involved in both experimental and modeling, a mean mechanical response of the SM micro-elements should be approached; in fact, the presence of some lacks of uniformity in the material properties (i.e. grain size) as well as defects, derived from the fabrication processes (laser micro-cutting and chemical etching), could affect significantly the final mechanical response.

In order to considering these effects, the phenomenological approach, presented by Kohl et al. (1996), was implemented both for austenite and martensite for the mechanical modeling of the micro-elements, as depicted in Figure 3.

The first reason at the base of the use of this approach is for determinating the stress distribution in a geometry (i.e. micro-elements with snake like configuration) with curvatures, where the classical equations of load–stress cannot be easily applied. Moreover, the second reason is to model the mechanical behavior of micro-scaled elements presenting some potential geometrical or microstructural defects, due to the production route adopted for their realization. For instance, laser micro-processing can produce melted material, concentrated in some points of the geometry processed, and this can reduce the effectiveness of the next chemical etching for its polishing. As a result, localized areas of the sample surface may show not uniform mechanical behavior, which is seen as discontinuity in the material properties.

According to Kohl method, each point of the force versus displacement experimental curve $(\overline{d_i}, F_i)$ was considered as input for the FE modeling. An iterative calculation is then accomplished by the model; it consists in the determination of the elastic modulus E_i able to minimize the error $\left|d_i^* - \overline{d_i}\right|$ (here defined 2%), where d_i^* is the FEM output displacement related to E_i. In this way, for every $(\overline{d_i}, F_i)$, experimental point, a (d_i^*, F_i), modeled point is derived. By the entirety of the modeled force versus displacement points, the $(\sigma_i^*, \varepsilon_i^*)$, curve is then accomplished. After the stress versus strain response, the stress distribution is determined as output of the simulation.

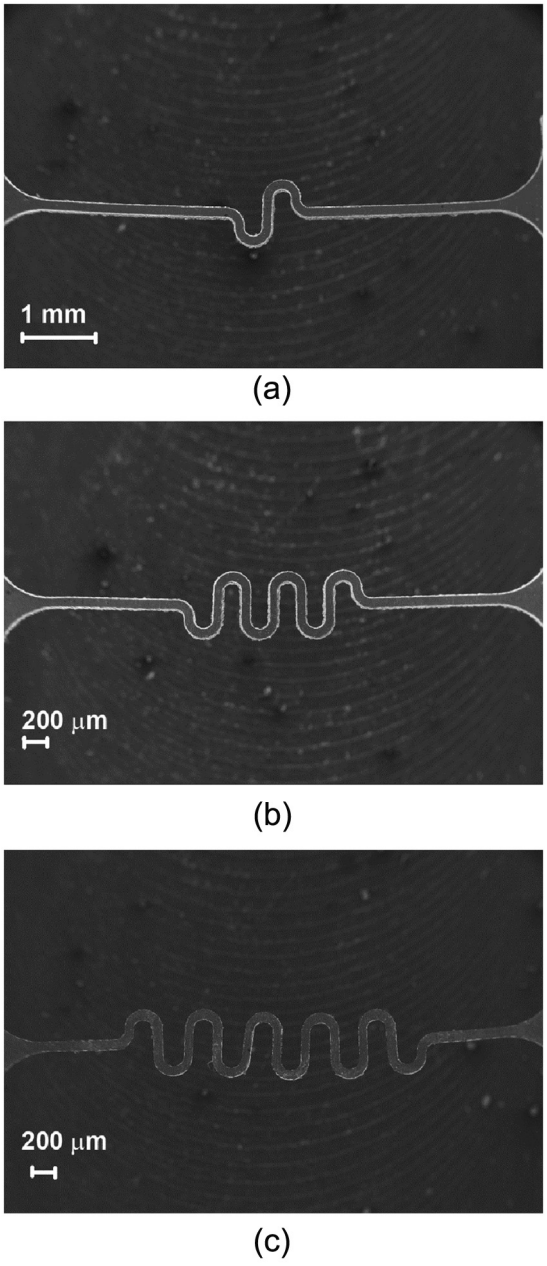

Figure 2. Geometry of the micro-elements at varying the number of curvatures M: (a) M = 1, (b) M = 3, and (c) M = 5.

This approach was adopted even in other works of the same authors, when samples with geometries far

Table 1. Characteristic dimensions of the micro-elements (mean and standard deviation) after their realization.

Height, h	Curvature radius, R	Width, w	Thickness, t
596.3 ± 2.7 μm	90.2 ± 1.9 μm	81.6 ± 1.3 μm	95.7 ± 1.5 μm

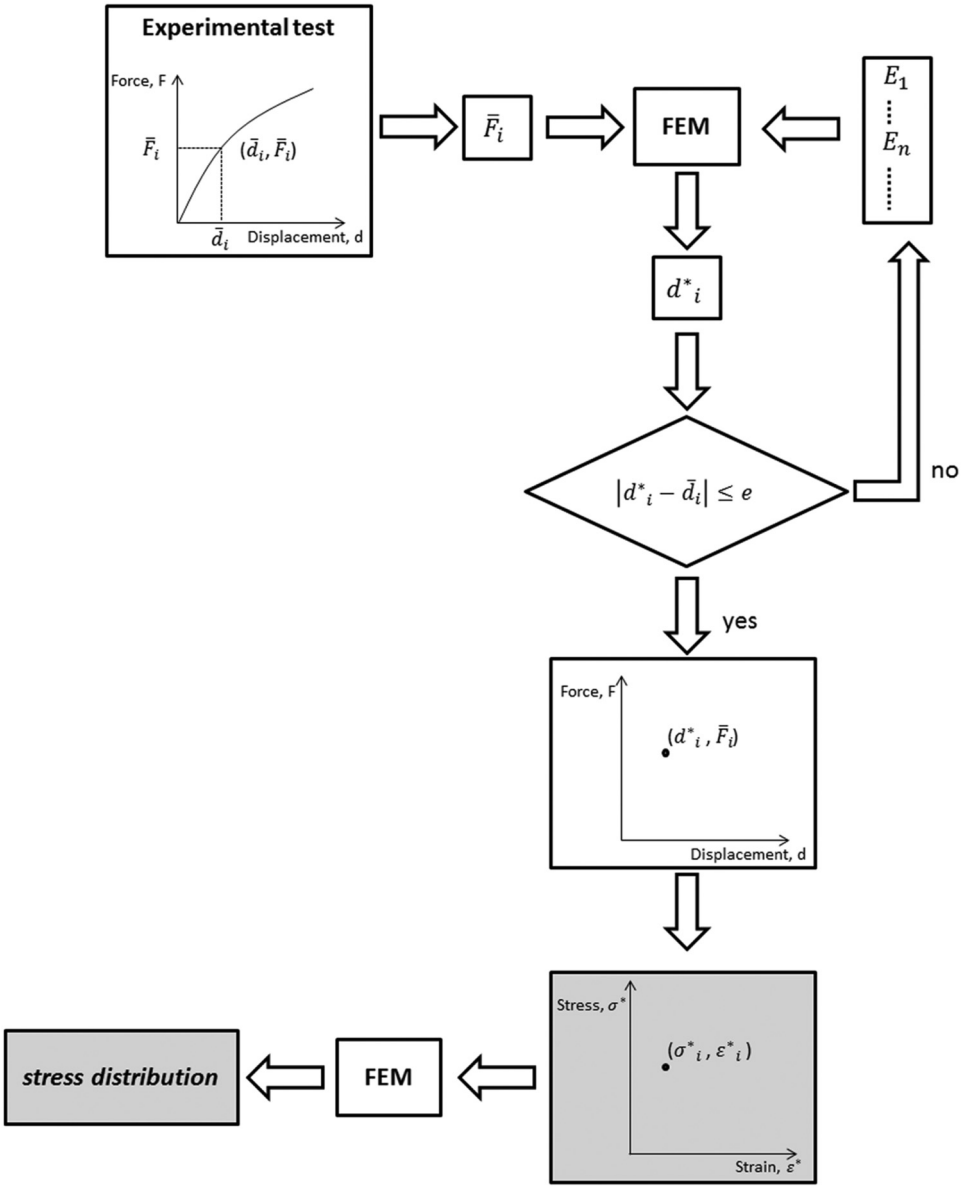

Figure 3. Schematic of the implementation of Kohl's phenomenological approach.

from the so-called "dogbone" geometry were numerically simulated (Kohl and Skrobanek, 1998). The two main hypotheses at the basis of this FEA are the following: (1) isotropic and uniform properties of the material and (2) rectangular transversal section of the micro-elements.

The modeling was performed under steady-state condition at two different temperatures, below (−20°C) and above (70°C) the MT, at which the elastic stiffness, indicated as Young modulus E, can be directly associated with the pure martensitic and austenitic phases. Here, the presence of the stress-induced martensite (SIM) was not taken into account, because in this preliminary approach the micro-elements were used at low values of force applied.

Coupling both Kohl's approach and FEA modeling, two outputs can be obtained: (1) the stress–strain curve, characteristic of each micro-element tested in the first part of this work and (2) the corresponding stress distribution in function of M, as reported in the gray blocks.

Analysis of results

Figure 4 shows the DSC heating/cooling scans of a micro-element. Martensite start and finish temperatures (Ms and Mf) and the austenite (As and Af) temperatures as well as transformation heats were detected, and the values are reported in Table 2. The thermal hysteresis, obtained from the DSC scan of Figure 4, was

Table 2. Characteristic temperatures of the MT of the micro-elements, from DSC analysis and from strain recovery test at the correspondence of the 1st and 30th cycles.

Testing	As (°C)	Af (°C)	$H^{M\rightarrow A}$ (J/g)	Ms (°C)	Mf (°C)	$H^{A\rightarrow M}$ (J/g)	Thermal hysteresis (°C)
DSC	40	46	19.4	18	14	20.3	27
ε recovery (1st cycle)	59	81	–	10	3	–	70
ε recovery (30th cycle)	48	67	–	15	7	–	56

MT: martensitic transformation; DSC: differential scanning calorimetry.

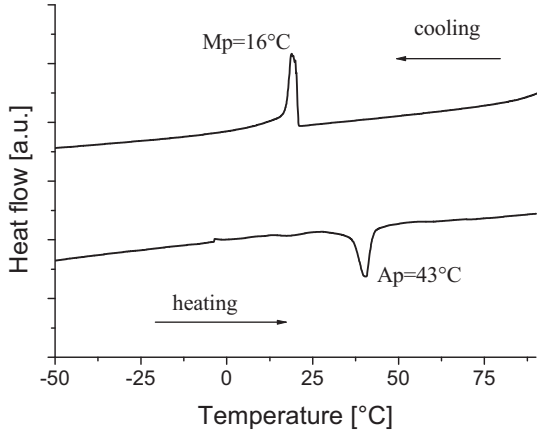

Figure 4. Representative DSC scan of the NiTi micro-elements.

about 27°C, which is comparable with the thermal hysteresis of commercial NiTi SMA for actuators.

The knowledge of the characteristic temperatures derived from the DSC measurement allows carrying out the mechanical characterization, through tensile testing, of the micro-elements in the two material states: in martensite, below the conclusion of the direct MT (see Mf), and in austenite, above the conclusion of the reverse MT (see Af).

Martensite and austenite mechanical response of the micro-elements with M = 1, 3, 5 (see Figure 2) was obtained at the testing temperatures below (−20°C) and above (70°C) the MT. Figure 5 shows the mechanical behaviors up to the failure of the micro-elements. Because of the "snake-like" geometry of the samples, the results of the tensile testing were reported as force–displacement response, instead of stress–strain curve.

As expected, martensite and austenite show different mechanical response in terms of Young's modulus, stress plateau, maximum stress, and displacement. The relevant level of stroke in correspondence to the failure of the elements according to the increase in M can also be detected. This can be explained since the elongation of these micro-elements can be seen similarly with the elongation of a bidimensional spring. The generation of SIM in the curves of the austenite in correspondence to the change in curvature in the force–displacement results can also be seen.

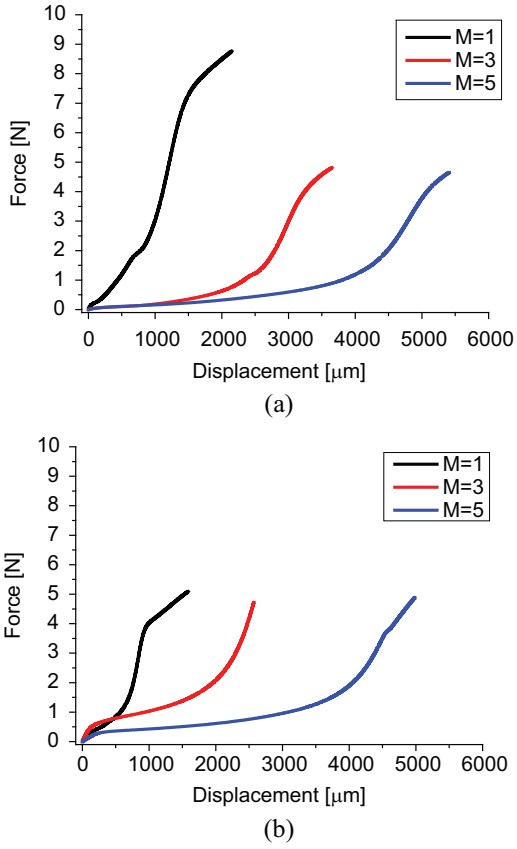

Figure 5. Force–displacement curves at temperatures (a) below the MT and (b) above the MT.

A decrease in the maximum force, before the element failure, is visible in the martensitic phase from about 9 to 5 N at increasing M, while in the austenitic phase the variation in the maximum force is more limited in the range 5–6 N. Even if the mechanical tests are performed at different temperatures, the material condition seems not to influence the maximum force at the failure in the case of the micro-element with M = 5.

Moreover, strain recovery tests were also performed at prefixed values of applied load. A representative cycling, showing the evolution of the performances of the micro-element with M = 5, is shown in Figure 6.

During the thermal cycling (30 cycles), the applied load is fixed equal to 0.1 N, and heating/cooling loops

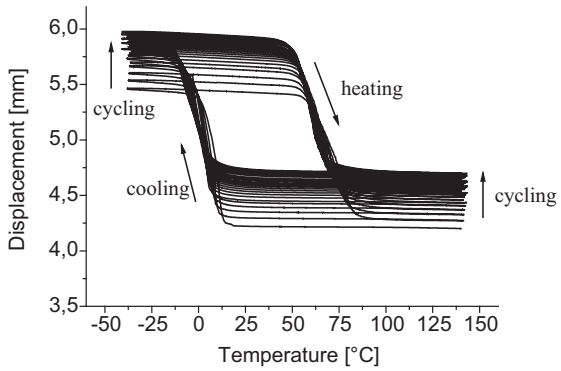

Figure 6. Displacement recovery cycling of micro-elements with M = 5 (applied load of 0.1 N).

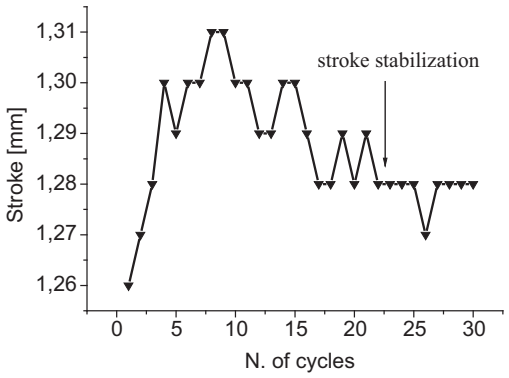

Figure 7. Evolution of the stroke during thermal cycling (micro-element with M = 5; applied load of 0.1 N).

were imposed to guarantee the complete transformation from austenite to martensite, and vice versa. The displacement recovery, shown in Figure 6, was actuated by the SM effect. The micro-element shows an important stroke of about 1.2 mm (equivalent to the 42% of the initial length), evaluated as difference between the minimum and maximum displacements.

An initial thermal cycling is required to reach the stabilization of both minimum and maximum displacements (see evolution in Figure 6) and the relative stroke (see evolution in Figure 7). Indeed, approximately 22 cycles are required to reach a stable behavior, as indicated by the arrow drawn in Figure 7.

Nonetheless, during this test, austenite and martensite accumulate a similar level of plastic deformation, that is, about 0.5 mm by the 30th cycle, because of the translation of the stroke at higher values. Moreover, the finish transformation temperature Af is shifted to higher values, if compared with the temperatures measured by the DSC scan (see Table 2). The reason of this shift is due to the applied forces, which can modify the characteristic temperatures of the MT, according to the Clausius–Clapeyron relationship. On the contrary, this trend was not observed for Mf; this point needs further investigations for its clarification. An increase in the thermal hysteresis, under load, has also been obtained; this behavior could be probably associated with the lack of uniform stress distribution for the presence of the curvatures.

After the testing of these micro-elements, an estimation of the stress distribution can be another important issue for completing their characterization. For applying the phenomenological approach, described and used by Kohl et al. (1996), the experimental response of the device is required. For this purpose, the force–displacement curves, suitable for the use of the micro-elements, should be focalized in the range of low forces, as depicted in Figure 8. For temperature above Af, the displacement of the three micro-elements (M = 1, 3, and 5) increases proportionally with the force applied.

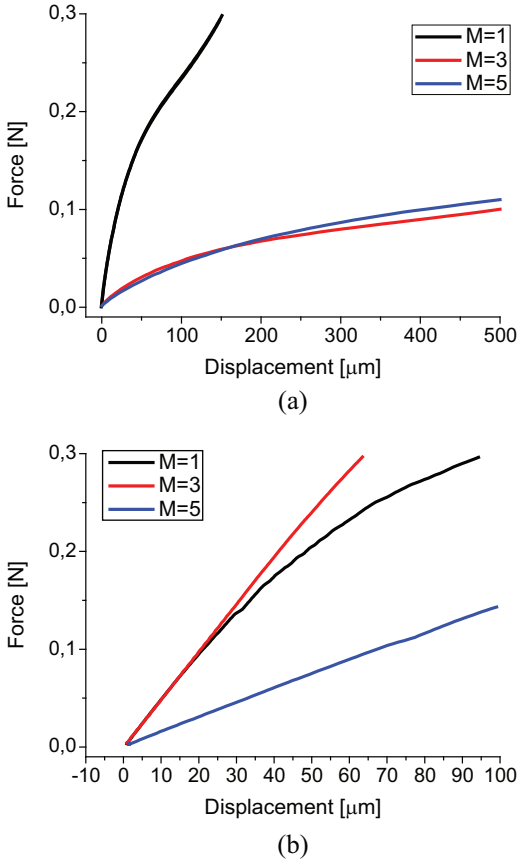

Figure 8. Experimental force–displacement curves at temperatures (a) below and (b) above the MT, in the range of stroke of use of the micro-elements.

The punctual inclination of the force–displacement curve is proportional to the Young's modulus; it is confirmed from this measurement that the austenitic phase shows a higher Young's modulus than the martensitic one. On the contrary, the mechanical response of the martensitic phase shows a trend between force and

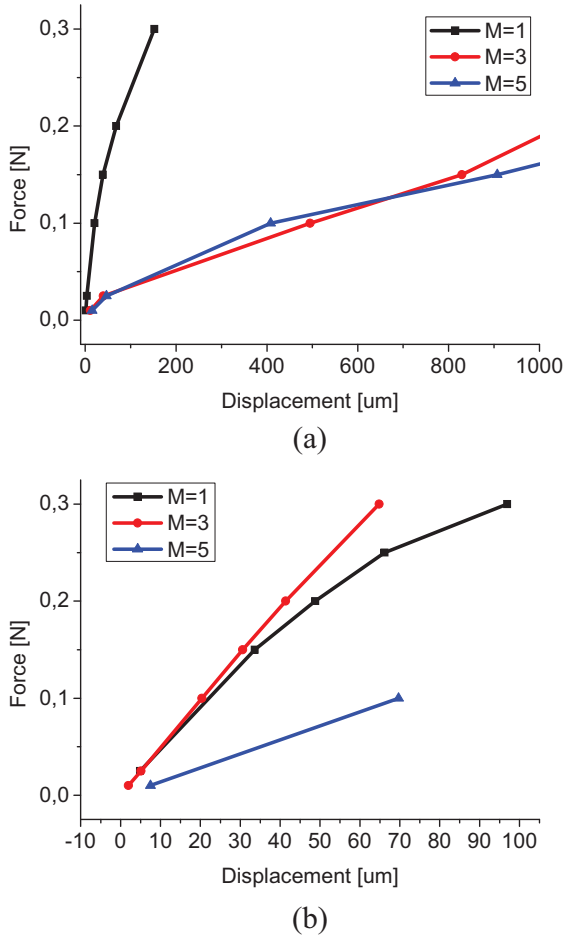

Figure 9. Calculated force–displacement curves at temperatures (a) below and (b) above the MT by applying Kohl's approach.

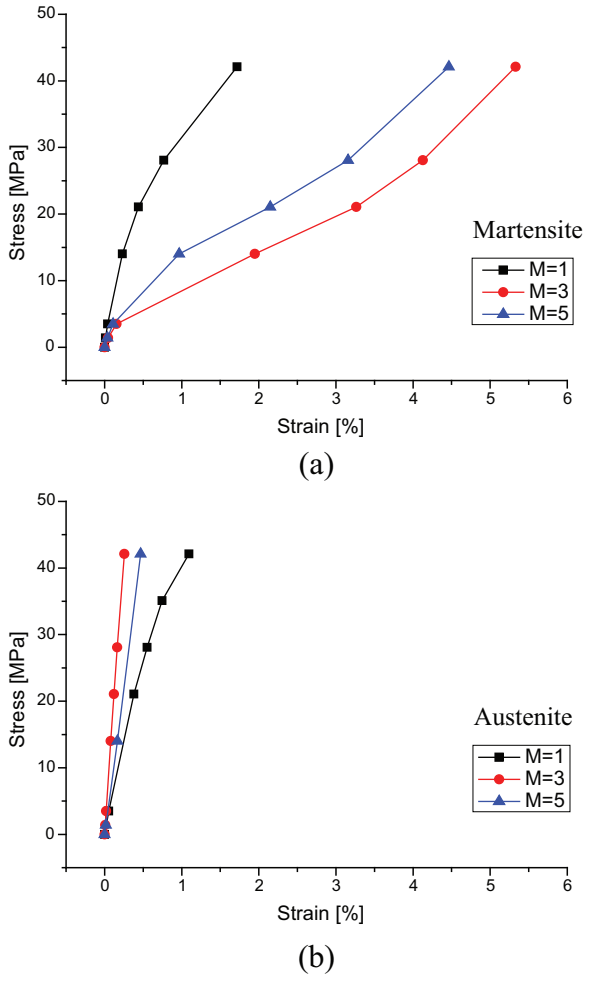

Figure 10. Calculated stress–strain characteristics from FEA at temperatures (a) below and (b) above the MT for micro-elements with M = 1, 3, 5.

displacement, characterized by a lower modulus. This behavior can be confirmed by literature (Rajagopalan et al., 2005). These curves, depicted in Figure 8, were used as input for the FEA of the micro-elements.

In Figure 9, the calculated force–displacement curves are depicted; due to the fact that the curves of Figure 8 were used as input for the iterative calculation, depicted in Figure 3, the difference between the force–displacement curves of Figures 8 and 9 is given by the error defined. In fact, the trend among the force–displacement curves, experimental and calculated, is definitely the same.

Figure 10 shows the calculated stress–strain characteristics, representative for the different geometries in both martensitic and austenitic phases. The results reported in the plots of Figure 10 are representative of the average stress, like the element would be straight linear with uniform stress distribution. This result shows that the Young's modulus is represented by a polynomial line and not just by a linear line. According to the experimental results, it can be seen that the Young's modulus is higher in the austenite state, even if it seems to be influenced by the parameter N, too. Moreover, the Young's modulus can be directly calculated from the curves of Figure 10, instead of qualitative information which was associated with the curves of Figure 8. It can be seen that the stress–strain characteristics of Figure 10 show a certain variation for both the martensitic and austenitic states. In particular, it was noted that the stress–strain characteristic of the micro-element with M = 1 seems to be far from the other ones from a qualitative point of view. Besides, the numerical difference on the estimation of the Young's modulus is also quite evident, as it can be seen in Figure 10. This difference in the mechanical response could be explained through some reasons: (1) the presence of some defects, introduced during the fabrication steps and (2) variability of the material behavior.

The trends of the calculated stress–strain curves are compatible with the literature, like that reported in [9], while the modulus values are not in some conditions. The authors can report some hypothesis about the

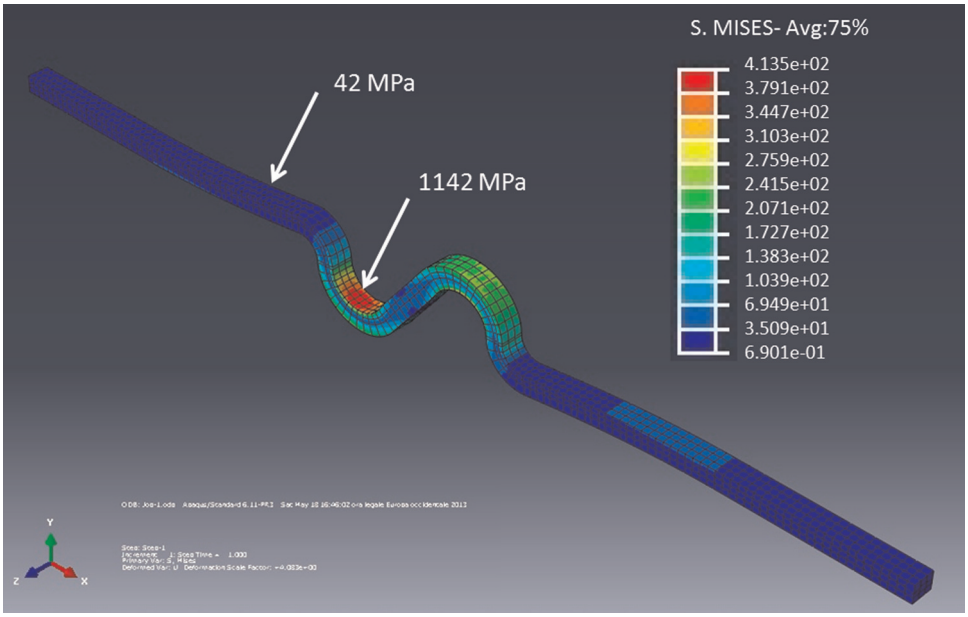

Figure 11. von Mises stress distribution in the micro-element with M = 1 at F = 0.3 N.

reason of this difference between the modulus calculated and reported by the literature. The most reasonable hypothesis about the reason of this difference between the modulus calculated and reported by the literature is that some localized effect, far from the macro behavior, can be associated with. This can also be confirmed by Rajagopalan et al. (2005). It is reported that the stress–strain curves of martensitic NiTi using macroscopic extensometry include strain from twinning that results in a significant low Young's modulus, which are not truly representative of elastic deformation. The macroscopic measurements resulted in a modulus of 68 GPa, significantly less than the 101 GPa from indentation and the lattice plane average of 109 GPa from neutron diffraction. This difference should be due to microeffects, measured by the indentation and neuron diffraction characterizations, not detectable by macroscopic techniques. In the case of this work, this large difference among moduli can be associated with microeffects, depending on the micro range of the micro-elements, while common literature reports Young's modulus, obtained by tensile test on significantly larger samples with the traditional dogbone geometry. Moreover, the authors would underline also that the variability of the procedure of realization of these micro-elements (rolling, laser cutting and etching) does influence the final performances, shown in the experimental testing, from which the Young's modulus was calculated. According to the stress–strain characteristic of the current micro-element, the corresponding stress distribution was proposed. The simulated stress distribution in the micro-element with M = 1 and M = 5 is shown in Figures 11 and 12, respectively.

The stress distribution is not uniformly distributed in the semi-circular part of the micro-element, as it could be expected, because of the generation of both axial and tangential stresses. It can be seen from Figures 11 and 12 that the stress concentration is localized at the internal surface of the semi-circular part of the micro-element. In fact, the stress can be increased from about 42 MPa in the blue colored surface (in correspondence to the straight linear part of the micro-element) to about 1142 MPa in the red colored surface with an applied load of 0.3 N (see arrows in Figure 11).

In Figure 12, the stress distribution is depicted in the micro-element with M = 5 at F = 0.1 N. The maximum von Mises stress is about 413 MPa at F = 0.1 N in correspondence to a displacement of about 400 μm.

Conclusion

In this work, a study of the thermo-mechanical performances of NiTi SM micro-elements was proposed. The results show that the number of curvatures N strongly influences the tensile behavior of the martensite and austenite phases. In particular, a reduction in the Young's modulus and an increase in the deformation up to fracture with increasing the number of curvatures M was observed. A large displacement recovery after a thermo-mechanical loop and a good cycling stability was also seen. FEM was used for realizing the stress–strain characteristic and for studying the stress distribution of the micro-elements as a function of the number of curvatures and as a function of the material state. The obtained stress–strain characteristics, numerically calculated, were seen to differ in function of the micro-element; this could

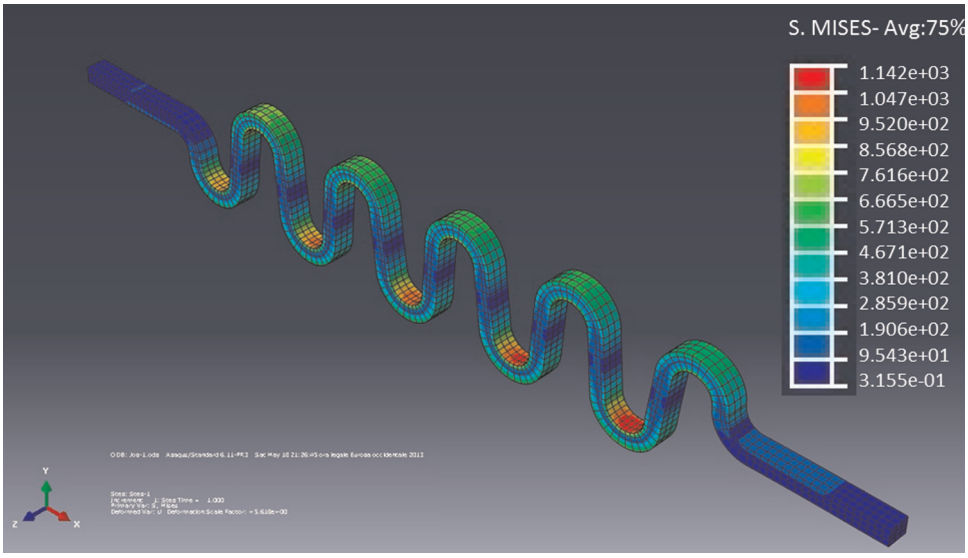

Figure 12. von Mises stress distribution in the micro-element with M = 5 at F = 0.1 N.

be explained through the presence of some defects (microstructural, geometrical) which increase the variability of material response. Later, the stress distribution was reported, showing the stress concentration at the internal semi-circular part of the micro-elements.

Acknowledgements

The authors wis h to thank Dr Elena Villa and Mr Giordano Carcano for their technical support in the experimentation.

Declaration of conflicting interests

The authors declared no potential conflicts of interest with respect to the research, authorship, and/or publication of this article.

Funding

This research received no specific grant from any funding agency in the public, commercial, or not-for-profit sectors.

References

Bellouard Y, Clave R, Gotthardt R, et al. (2008) Shape memory alloys for microsystems: a review from a material research perspective. *Materials Science and Engineering A* 481–482: 582–589.

Biffi CA, Bassani P, Carnevale M, et al. (2014) Effect of laser microcutting on thermo-mechanical properties of NiTiCu shape memory alloy. *Metals and Materials International* 20(1): 83–92.

Biffi CA, Bassani P, Tuissi A, et al. (2012) Flexural vibration suppression of glass fiber/CuZnAl SMA composite. *Functional Material Letters* 5(1): 12500142.

Biffi CA, Nespoli A, Previtali B, et al. (2013) NiTi shape memory elements for smart micro-actuation: laser processing, chemical etching and functional characterization. In: *6th ECCOMAS conference on smart structures and materials, Politecnico di Torino*, Torino, Italy, 24 June.

Funakubo H (1984) *Shape Memory Alloys*. London: Gordon & Breach Science Publishers.

Ikuta K (1990) Micro/miniature shape memory alloy actuator. In: *Proceedings of IEEE international conference on robotics and automation*, Cincinnati, OH, 13–18 May.

Kohl M and Skrobanek KD (1998) Linear microactuators based on the shape memory effect. *Sensors and Actuators A* 70: 104–111.

Kohl M, Krevet B and Just E (2002) SMA microgripper system. *Sensors and Actuators A* 97–98: 646–652.

Kohl M, Skrobanek KD, Goh CM, et al. (1996) Mechanical characterization of shape memory micromaterials. In: *Symposium on Micromachining and Microfabrication*, Austin, TX, 14 October, vol. 2880, pp. 108–118. USA: Spie.

Li C, Nikumb S and Wong F (2006) An optimal process of femtosecond laser cutting of NiTi shape memory alloy for fabrication of miniature devices. *Optics and Lasers in Engineering* 44: 1078–1087.

Nespoli A, Bassani E, Besseghini S, et al. (2010a) Rotational mini-actuator activated by two antagonist shape memory alloy wires. *Physics Procedia* 10: 182–188.

Nespoli A, Besseghini S, Pittaccio S, et al. (2010b) The high potential of shape memory alloys in developing miniature mechanical devices: a review on shape memory alloy mini-actuators. *Sensors and Actuators A* 158: 149–160.

Nespoli A, Biffi CA, Casati R, et al. (2012a) New developments on mini/micro shape memory actuators. In: G Berselli, R Vertechy and G Vassura (eds) *Smart Actuation and Sensing Systems: Recent Advances and Future Challenges*. Rijeka: Intech, pp. 35–52.

Nespoli A, Biffi CA, Previtali B, et al. (2014) Laser and surface processes of NiTi shape memory elements for micro-actuation. *Metallurgical and Materials Transactions A* 45(4): 2242–2249.

Nespoli A, Villa E and Besseghini S (2012b) Thermo-mechanical properties of snakelike NiTi wires and their use in

miniature devices. *Journal of Thermal Analysis and Calorimetry* 109: 39–47.

Otsuka K and Wayman CM (1998) *Shape Memory Materials*. Cambridge: Cambridge University Press.

Pfeifer R, Herzog D, Hustedt M, et al. (2010) Nd:YAG laser cutting of NiTi shape memory alloys—influence of process parameters. *Journal of Materials Processing Technology* 210: 1918–1925.

Previtali B, Arnaboldi S, Bassani P, et al. (2010) Microcutting of NiTiCu alloy with pulsed fiber laser. In: *10th Biennial conference on engineering systems design and analysis*, Istanbul, 12–14 July.

Rajagopalan S, Little AL, Bourke MAM, et al. (2005) Elastic modulus of shape-memory NiTi from in situ neutron diffraction during macroscopic loading, instrumented indentation, and extensometry. *Applied Physics Letters* 86(8): 081901.

Schuessler A (2000) Laser processing of nitinol materials. In: *Proceedings of SMST*, Pacific Groove, CA, USA, 30 April - 4 May, pp. 25–32.

Tuissi A, Besseghini S, Ranucci T, et al. (1999) Effect of Nd:Yag laser welding on the functional properties of the Ni-49.6at%Ti. *Materials Science and Engineering A* 273–275: 813–817.

Yung KC, Zhu HH and Yue TM (2005) Theoresing 355 nm Nd:Yag. *Smart Materials and Structures* 14: 337–342.